Title

Measurements of electron temperature in high-energy-density plasmas using gated x-ray pinhole imaging

Journal

REVIEW OF SCIENTIFIC INSTRUMENTS, 92(4)

ISSN

0034-6748

Authors

Schaeffer, DB
Fox, W
Rosenberg, MJ
et al.

Publication Date

2021

DOI

10.1063/5.0043833

Measurements of Electron Temperature in High-Energy-Density Plasmas using Gated X-Ray Pinhole Imaging

D. B. Schaeffer,[1, a)] W. Fox,[1, 2] M.J. Rosenberg,[3] H.-S. Park,[4] G. Fiksel,[5] and D. Kalantar[4]
[1)] *Department of Astrophysical Sciences, Princeton University, Princeton, NJ 08540 USA*
[2)] *Princeton Plasma Physics Laboratory, Princeton, New Jersey 08543 USA*
[3)] *Laboratory for Laser Energetics, University of Rochester, Rochester, NY 14623 USA*
[4)] *Lawrence Livermore National Laboratory, Livermore, CA 94550 USA*
[5)] *Center for Ultrafast Optical Science, University of Michigan, Ann Arbor, MI 48109 USA*

(Dated: 20 March 2021)

We present measurements of spatially- and temporally-resolved electron temperature in high-energy-density (HED) plasmas using gated x-ray pinhole imagers. A 2D image of bremsstrahlung x-ray self-emission from laser-driven plasma plumes is detected at the same time through two pinholes covered with different filter materials. By comparing the attenuated signal through each filter, a spatially-resolved electron temperature as low as 0.1 keV can be estimated. Measurements of the plasma plume taken from different directions indicate that imaging through extended plasmas has a negligible effect on the temperature estimates. Methods for estimating the expected signal, selecting filters, and incorporating the response of the detector are discussed.

I. INTRODUCTION

X-ray Bremsstrahlung measurements are a common method of diagnosing electron temperatures in laser-produced plasmas. Many applications of x-ray measurements, such as inertial confinement fusion on the National Ignition Facility (NIF), are concerned with x-rays of several keV or higher. These can be diagnosed directly with x-ray spectrometers[1,2], or imaged onto an image plate or CCD through a differential Ross pair filter[3,4] to extract temperatures. Applications with colder plasmas, however, are not well-served by these techniques, as both are insensitive to x-ray energies below a few keV.

By instead comparing the attenuated x-ray signal through two different filters, electron temperatures down to 0.1 keV can be measured. Unlike a Ross pair filter, which targets a narrow energy band, this technique can cover a wide range of energies for a given filter pair. Additionally, the filters can be paired with a gated pinhole camera to provide both spatial and temporal resolution.

II. DIAGNOSTIC SETUP

The measurements were performed with the Gated X-ray Detector (GXD) as part of Discovery Science experiments[5] on the NIF. A schematic of the setup is shown in Fig. 1a. Two lines of 20 drive beams (100 J/beam, 0.6 ns square pulse) irradiated a high-density carbon (HDC) target foil, which created two extended plasma plumes that expand away from the target. A GXD mounted on a Diagnostic Instrument Manipulator (DIM) viewed the plasmas from two equatorial angles: a face-on view from DIM 90-078 and an oblique side-on view from DIM 90-124. The pinholes on DIM 90-078 were positioned 478 mm from the target center, and the image plane was 836 mm behind the pinholes, for a total magnification of 1.75×. The pinholes on DIM 90-124 were positioned 669 mm from the target center, and the image plane was 836 mm behind the pinholes, for a total magnification of 1.25×. A 0.5 mm diameter aluminum torus wrapped around most of the target to shield diagnostics from the intense x-rays created near the target surface. The shield partially blocked 0.25 mm of the plasma plumes vertically in the 90-124 view.

The GXD consists of a pinhole array with filters, a micro-channel plate (MCP) with four embedded striplines, and a CCD camera[6] (see Fig. 1b). The striplines allow for sequential x-ray images, where each strip can have an independent trigger delay and covers approximately 250 ps from one end of the strip to the other. For these measurements the strips were timed in pairs, such that the first two strips had one trigger delay, and the second two strips had different trigger delay. Similarly, each pair of strips had the same bias voltage, which sets the gain. The 90-78 GXD was gated for approximately 600 ps, while the 90-124 GXD was gated for approximately 200 ps.

Over six NIF shots a variety of filter materials were used for each GXD. For all, the filters completely covered the corresponding pinholes. The pinholes were arranged so that the pinhole images that were projected onto the CCD were centered on, and spaced evenly along, the strips. Consequently, images through corresponding pinholes on each strip in a pair were acquired at the same time. All pinholes were 150 μm in diameter on a 75 μm thick Ta substrate. Both in front and behind the pinhole array was a corresponding array of 300 μm diameter collimator holes on a 500 μm thick Ta substrate. Some filters were built up in layers, so that one material would cover all pinholes, and another material would cover a subset of pinholes. For filters less (greater) than 10 μm thick, the filter thickness was measured to an accuracy of 0.1 (1) μm, and the pinhole diameters were measured to an

[a)] Electronic mail: dereks@princeton.edu

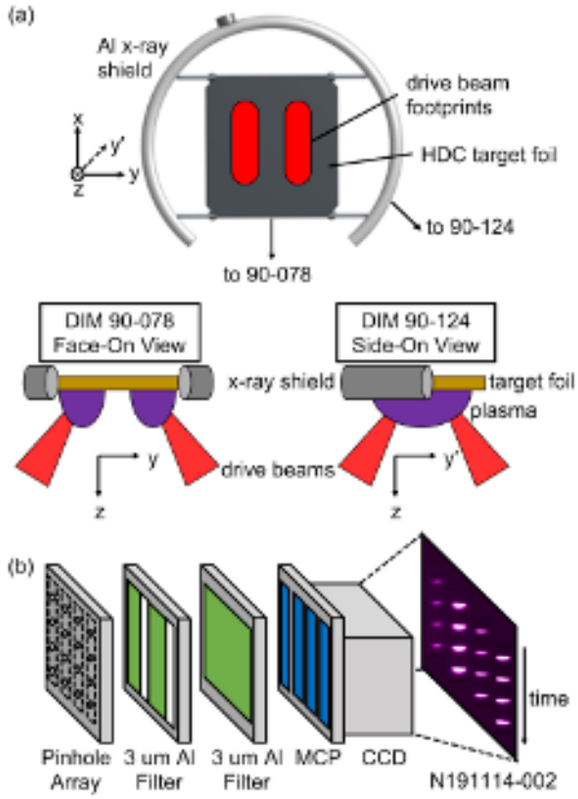

FIG. 1: (a) Schematic of the diagnostic setup on the NIF. An HDC target foil is placed in the equatorial plane and irradiated by beams arranged along two extended focal spots. An Al shield wraps around most of the target to block x-rays from the laser-target interaction. GXDs view the resulting expanding plasma plumes either face-on from DIM 90-078 or at an oblique side-on angle from DIM 90-124. (b) Diagram of the main components of the GXD with example 3 and 6 μm Al filtering.

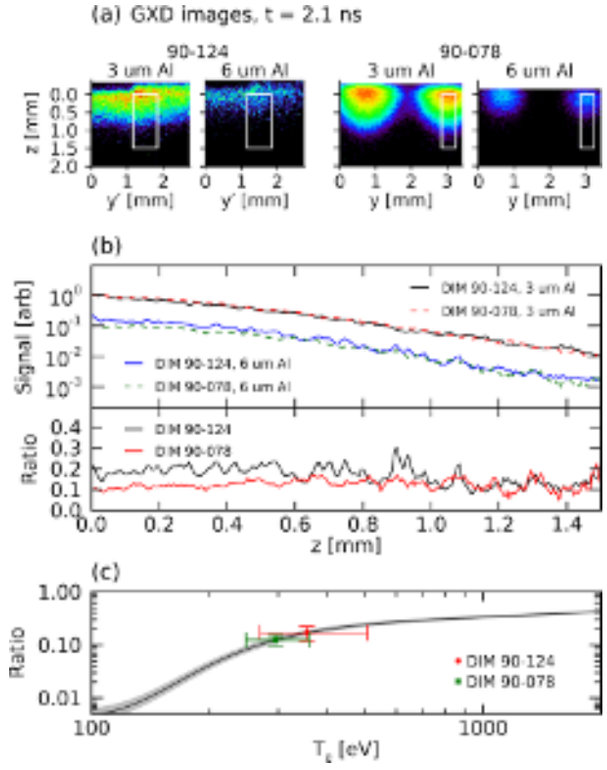

FIG. 2: Example temperature analysis using filtered gated x-ray pinhole images. (a) Two pairs of pinhole images taken 2.1 ns after the lasers fire. The left pair (side-on) was taken from a GXD in DIM 90-124 on shot N191114-002 and the right pair (face-on) from DIM 90-078 on shot N191114-001. Each pair consists of an image acquired through a 3 and 6 μm Al filter. White boxes indicate the regions of interest used to create lineouts in (b). The intensity values are logarithmically scaled. (b) Signal profiles from (a), normalized to the peak value of the 90-124 3 μm Al-filtered image, and the resulting ratio between the 6 and 3 μm Al-filtered images in each pair. (c) Calculated ratio from Bremsstrahlung emission through a 6 and 3 μm Al filter as a function of electron temperature (solid black line). The shaded region corresponds to the measurement uncertainty in the filter thickness. Overplotted are the average ratio values from (b) and associated uncertainties.

accuracy of 1 μm. Due to the large standoff distances of the detectors and the close spacing of the pinholes, parallax was negligible when comparing pinhole images.

The response of the detector varies differently along each strip, and is highly dependent on the individual GXD and strip bias voltages. Detector response and sensitivity were calibrated using a uniformly illuminated gold sphere and provided by NIF. As a result, only a subset of all possible combinations of detector parameters are explicitly calibrated. The experimental images were thus calibrated against flatfield images with similar (though not exact) parameters for that detector, including the same bias voltages. This allowed the signal response for each strip in a pair to be normalized for direct comparison. The flatfields were further validated by comparing the signals through two identically filtered pinholes on different strips for both uncalibrated and calibrated images. A background image was taken on each detector shortly before each data and calibration shot. After subtracting the background images, the data image was divided by the mean-normalized flatfield image to produce the final image used for analysis.

III. X-RAY ANALYSIS

To estimate the electron temperature, we utilize the fact that the same x-ray signal will be attenuated differently through two different filters. Here, we assume that the x-ray signal is due to Bremsstrahlung continuum emission from the plasma, for which the corresponding emissivity (power/unit frequency/unit volume) scales like $j(\nu) \propto \frac{n_e^2}{\sqrt{T_e}} \exp^{-h\nu/T_e}$[7], where ν is the frequency, n_e is the electron density, T_e is the electron temperature, and h is Planck's constant. The solid angle subtended by a pinhole of diameter a at a distance d from the target is well approximated as $\Omega_{ph} \approx \frac{\pi a^2}{4d^2}$. In our experiments n_e is typically of order or smaller than 10^{20} cm^{-3}[5], so that

the plasma is optically thin to Bremsstrahlung radiation at all times considered. The total number of x-ray photons per unit area dA incident on the detector through a pinhole is then $NdA = \frac{\Omega ph}{4\pi} V\tau dA \int j(\nu)K(\nu)d\nu$, where $K(\nu)$ is the detector MCP response per unit photon energy, τ is the total time photons are collected (set by the gate time of the detector), $V = \int dA' d\ell$, A' is the projected plasma area imaged through the pinhole, ℓ is the plasma length along the line-of-sight, and we have assumed there are no temperature gradients along ℓ.

By comparing the same Bremsstrahlung signal through two different filters, the plasma and diagnostic variables cancel out except for the dependence on temperature. Since only the frequency response will change between the two filters, the ratio of incident photons between two filters, denoted by subscripts 1 and 2, is

$$R = \frac{N_1}{N_2} = \frac{\int_0^\infty j(\nu)K(\nu)W_1(\nu)d\nu}{\int_0^\infty j(\nu)K(\nu)W_2(\nu)d\nu} \quad (1)$$

where W is the frequency-dependent attenuation response of the filter. The same ratio then applies to the GXD signal response, which is proportional to the number of incident photons within the linear regime of the detectors[8].

An example analysis is shown in Fig. 2 for GXD images taken 2.1 ns after the lasers fire (and 1.5 ns after the end of the laser pulse) from two NIF shots. Fig. 2a shows two pinhole images from NIF shot N191114-002 from DIM 90-124 ("side-on") taken through a 3 and 6 μm Al filter foil, and two images from DIM 90-78 ("face-on") taken through similar filters on shot N191114-001 with the same parameters. The plasma plumes expand vertically downward along z. Lineouts centered on the plumes and averaged over approximately 300 μm in y are shown in Fig. 2b for all images in Fig. 2a (white boxes). The lineouts are aligned starting at the peak value ($z = 0$) and extend 1.5 mm along z. To compare signals between GXDs, the lineouts are normalized to the peak value from the 3 μm Al side-on image. The ratio between the 6 and 3 μm Al images is also shown for each image pair. In principle, temperature gradients along the plume profiles are detectable as gradients in the ratio profiles; however, in practice the ratios were nearly constant over the whole spatial range, with an average ratio of $\overline{R}_{90\text{-}124} = 0.169 \pm 0.051$ and $\overline{R}_{90\text{-}078} = 0.124 \pm 0.028$ for the 90-124 and 90-078 views, respectively.

Numerically evaluating Eq. 1, the ratio between a 6 and 3 μ Al filter foil as a function of electron temperature is shown in Fig. 2c. Here, we use x-ray data from Ref. 9 to get the transmission vs energy $W(\nu)$. MCP response vs energy $K(\nu)$ is derived from Ref. 10. The shaded region corresponds to the measurement uncertainty in the filter thickness. Overplotted are the average ratio values from Fig. 2b. The vertical error bars correspond to a combination of uncertainties in the ratio value, including the standard deviation from averaging the ratio value along the lineout, a 50 μm alignment uncertainty in the relative position of the lineouts for each image pair, and the measurement uncertainty in the pinhole diameter size. This range of ratio values is then used to estimate the temperature uncertainty by taking the minimum and maximum temperatures in the shaded region associated with the minimum and maximum ratio values. The average temperature values are then $\overline{T}_{e,90\text{-}124} = 360^{+150}_{-90}$ eV and $\overline{T}_{e,90\text{-}078} = 300^{+60}_{-50}$ eV, with the uncertainty dominated by the signal noise.

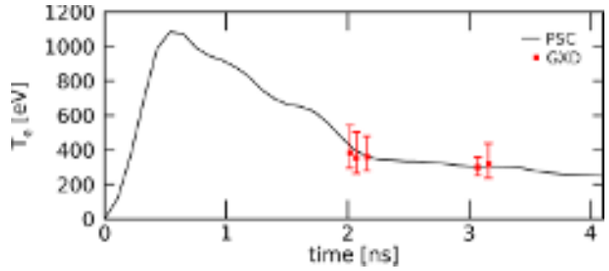

FIG. 3: Comparison of GXD-measured electron temperatures to particle-in-cell simulations with PSC.

There are two important features in these example images. The first is that for both the side-on and face-on views, the ratio value is nearly constant over 1.5 mm, implying that all of the signal variation in this region is due only to density gradients. The second is that viewing from side-on or face-on yields nearly identical signal profiles and similar temperature estimates, even between two separate shots. This implies that the plasma parameters are reproducible over multiple NIF shots, and that the line-of-sight integration does not significantly affect the temperature estimates. This is reasonable, since we expect both plasma plumes to behave similarly before they interact, and so only the total number of collected photons would change with line of sight. These two features also justify our earlier assumption that temperature gradient effects are negligible at the times and locations we measure.

The GXD-measured temperatures were compared to particle-in-cell simulations using the code PSC[11], as shown in Fig. 3. The simulations do not directly model the laser-target interaction, but instead incorporate a heating operator that mimics laser ablation. The resulting hydrodynamic evolution is well-matched to the output from separate radiation-hydrodynamic simulations of the laser-target interaction at the same parameters using the code DRACO[12]. At the same time, the PSC simulations can be run long enough to capture kinetic effects as the plumes begin to interact with one another. The GXD measurements are in excellent agreement with the simulation predictions between 2-3 ns after lasers turn on.

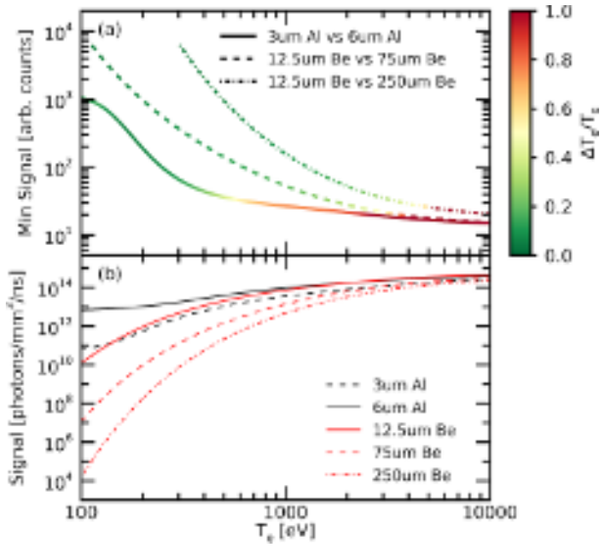

FIG. 4: (a) Plot of minimum signal value through a thin filter required to detect a signal value of 10 counts through the thicker filter, as a function of electron temperature, for three filter combinations. The lines are colored by the expected temperature resolution $\Delta T_e/T_e$ assuming a 25% uncertainty in the ratio value for each filter pair (saturated at $\Delta T_e/T_e = 1$ for clarity). (b) Individual signal responses $S = \int_0^\infty j(\nu)K(\nu)W(\nu)d\nu$ for different filters.

IV. DISCUSSION AND CONCLUSIONS

The Al filters discussed in the previous section were chosen because they were easily attainable, and maximized the collected signal while providing sufficient signal contrast and temperature resolution near the expected temperature value of a few hundred eV. Consequently, these filters would not be suitable if higher temperatures are expected, since at that point the ratio curve flattens out and even small changes in signal ratio would lead to large changes in estimated temperature, as can be seen in Fig. 2c. This is further demonstrated in Fig. 4a for three different filter combinations: 3 and 6 μm Al, 12.5 and 75 μm Be, and 12.5 and 250 μm Be. In units of CCD counts, the plots show the minimum signal required through the thinner filter in each pair to allow a detectable signal of 10 counts through the thicker filter, as a function of electron temperature. The profiles are further colored by the corresponding temperature resolution $\Delta T_e/T_e$, assuming a ratio uncertainty of 25% typical for the data. The profiles in Fig. 4a are based on the ratio from Eq. 1, while individual filtered responses are shown in Fig. 4b for an assumed density $n_e = 10^{20}$ cm^{-3}.

For the Al filters (solid line), temperatures below ~ 600 eV are well-resolved ($\Delta T_e/T_e < 0.5$), but require increasingly larger signal ratios at lower temperatures. The cause of both effects can be seen in Fig. 4b. A larger contrast between the filtered responses at lower temperatures results in better temperature resolution, while at higher temperatures the two responses are nearly identical. Conversely, the overall number of emitted photons is significantly lower at lower temperatures. Higher temperatures up to ~ 2 keV can be measured by using the 12.5 and 75 μm Be filters (dashed line), but at the cost of a required increase in collected photons to compensate for the thicker filters. By increasing the difference between the Be filter thicknesses (dot-dashed line), even higher temperatures can be measured, but it becomes no longer possible to measure the lower temperatures, regardless of x-ray intensity, since the required minimum signal exceeds the linear regime on the CCD detectors (approximately 10k counts for the GXD detectors on NIF). Increasing the thickness of the thinner filter, in turn, would reduce the minimum required signal, but at the cost of a reduced maximum resolvable temperature. In general, the widest resolvable temperature range will come from the largest possible difference in filter thickness that still allows measurable signals through both filters.

Through appropriate selection of filters, this diagnostic can thus cover a wide range of electron temperatures down to 0.1 keV that are not easily accessible with other x-ray diagnostics. A given filter pair is also generally sensitive to a broad energy range, providing flexibility when attempting to measure an unknown temperature. Over the timescales studied, measurements from multiple viewpoints and over multiple shots indicate that the diagnostic is robust to temperature fluctuations along the line-of-sight; alternatively, stronger line-of-sight effects could be accounted for by incorporating a model of temperature gradients into Eq. 1. Key to minimizing the effects of temperature gradients was the use of a CCD paired with a gated MCP, which localized the measurements to timescales shorter than the hydrodynamic time, while also providing spatial resolution.

V. DATA AVAILABILITY

The data that support the findings of this study are available from the corresponding author upon reasonable request.

ACKNOWLEDGMENTS

We thank the NIF Discovery Science Program for facilitating these experiments. Support for these experiments has been provided by the U.S. DOE, Office of Fusion Energy Sciences under FWP SW1626 FES. This work was performed under the auspices of the U.S. DOE by Lawrence Livermore National Laboratory under contract DE-AC52-07NA27344 and under DOE Award Nos. DE-SC-0016249 and DE-NA-0003856, and Field Work Proposal No. 4507 under DOE Contract No. DE-AC02-09CH11466.

[1]E. L. Dewald, K. M. Campbell, R. E. Turner, J. P. Holder, O. L. Landen, S. H. Glenzer, R. L. Kauffman, L. J. Suter, M. Landon,

M. Rhodes, and D. Lee, Review of Scientific Instruments **75**, 3759 (2004).
[2]F. Pérez, G. E. Kemp, S. P. Regan, M. A. Barrios, J. Pino, H. Scott, S. Ayers, H. Chen, J. Emig, J. D. Colvin, M. Bedzyk, M. J. Shoup, A. Agliata, B. Yaakobi, F. J. Marshall, R. A. Hamilton, J. Jaquez, M. Farrell, A. Nikroo, and K. B. Fournier, Review of Scientific Instruments **85**, 11D613 (2014).
[3]S. Glenn, P. M. Bell, L. R. Benedetti, D. K. Bradley, J. Celeste, R. Heeter, C. Hagmann, J. Holder, N. Izumi, J. D. Kilkenny, J. Kimbrough, G. A. Kyrala, N. Simanovskaia, and R. Tommasini, in *Penetrating Radiation Systems and Applications XII*, Vol. 8144, edited by G. P. Grim and R. C. Schirato, International Society for Optics and Photonics (SPIE, 2011) pp. 75 – 82.
[4]T. Ma, N. Izumi, R. Tommasini, D. K. Bradley, P. Bell, C. J. Cerjan, S. Dixit, T. Döppner, O. Jones, J. L. Kline, G. Kyrala, O. L. Landen, S. LePape, A. J. Mackinnon, H.-S. Park, P. K. Patel, R. R. Prasad, J. Ralph, S. P. Regan, V. A. Smalyuk, P. T. Springer, L. Suter, R. P. J. Town, S. V. Weber, and S. H. Glenzer, Review of Scientific Instruments **83**, 10E115 (2012).
[5]W. Fox, D. B. Schaeffer, M. J. Rosenberg, G. Fiksel, J. Matteucci, H. S. Park, A. F. A. Bott, K. Lezhnin, A. Bhattacharjee, D. Kalantar, B. A. Remington, D. Uzdensky, C. K. Li, F. H. Séguin, and S. X. Hu, "Fast magnetic reconnection in highly-extended current sheets at the national ignition facility," (2020), arXiv:2003.06351.
[6]J. A. Oertel, R. Aragonez, T. Archuleta, C. Barnes, L. Casper, V. Fatherley, T. Heinrichs, R. King, D. Landers, F. Lopez, P. Sanchez, G. Sandoval, L. Schrank, P. Walsh, P. Bell, M. Brown, R. Costa, J. Holder, S. Montelongo, and N. Pederson, Review of Scientific Instruments **77**, 10E308 (2006).
[7]I. H. Hutchinson, *Principles of Plasma Diagnostics*, 2nd ed. (Cambridge University Press, 2002).
[8]J. Wiza, Nuclear Instruments and Methods **162**, 587 (1979).
[9]B. Henke, E. Gullikson, and J. Davis, Atomic Data and Nuclear Data Tables **54**, 181 (1993).
[10]G. A. Rochau, J. E. Bailey, G. A. Chandler, T. J. Nash, D. S. Nielsen, G. S. Dunham, O. F. Garcia, N. R. Joseph, J. W. Keister, M. J. Madlener, D. V. Morgan, K. J. Moy, and M. Wu, Review of Scientific Instruments **77**, 10E323 (2006).
[11]K. Germaschewski, W. Fox, S. Abbott, N. Ahmadi, K. Maynard, L. Wang, H. Ruhl, and A. Bhattacharjee, Journal of Computational Physics **318**, 305 (2016).
[12]W. Fox, J. Matteucci, C. Moissard, D. B. Schaeffer, A. Bhattacharjee, K. Germaschewski, and S. X. Hu, Physics of Plasmas **25**, 102106 (2018).

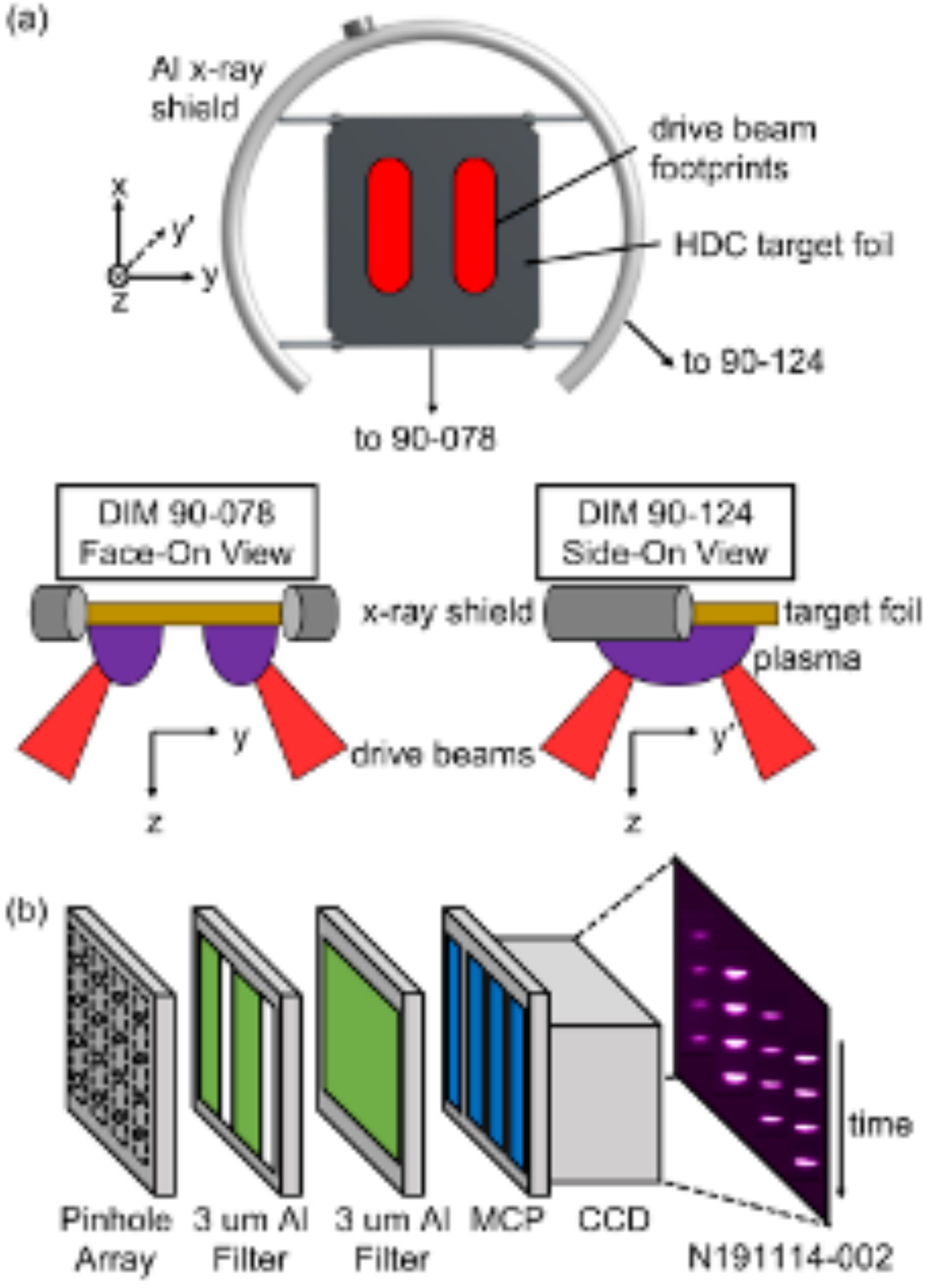
(a)
Al x-ray shield
drive beam footprints
HDC target foil
to 90-124
to 90-078
x
y'
y
z
DIM 90-078 Face-On View
DIM 90-124 Side-On View
x-ray shield
target foil
plasma
drive beams
y
z
y'
z
(b)
Pinhole Array
3 um Al Filter
3 um Al Filter
MCP
CCD
time
N191114-002

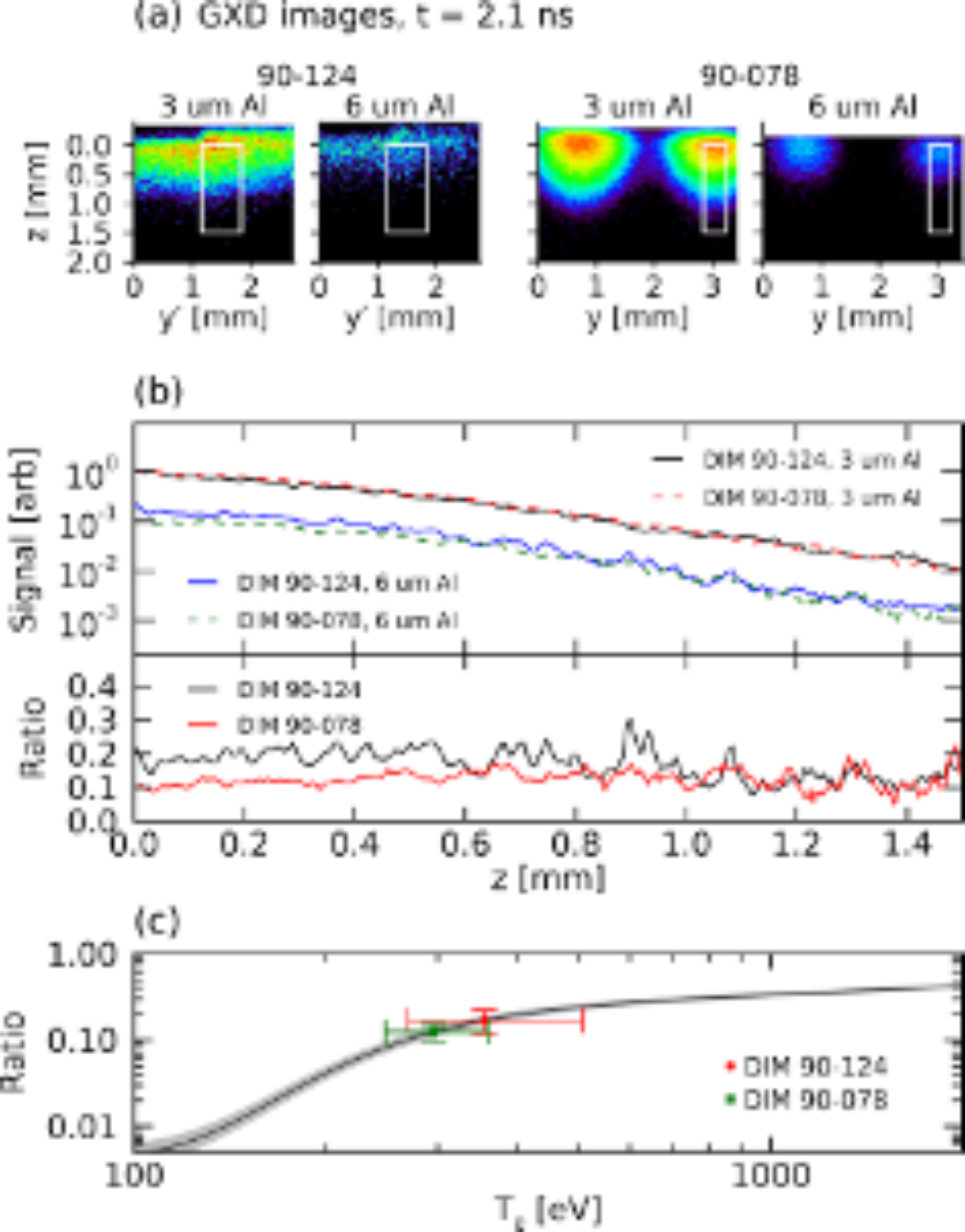
(a) GXD images, t = 2.1 ns
90-124
3 um Al
6 um Al
90-078
3 um Al
6 um Al
z [mm]
y' [mm]
y [mm]
(b)
Signal [arb]
DIM 90-124, 3 um Al
DIM 90-078, 3 um Al
DIM 90-124, 6 um Al
DIM 90-078, 6 um Al
Ratio
DIM 90-124
DIM 90-078
z [mm]
(c)
Ratio
DIM 90-124
DIM 90-078
T_e [eV]

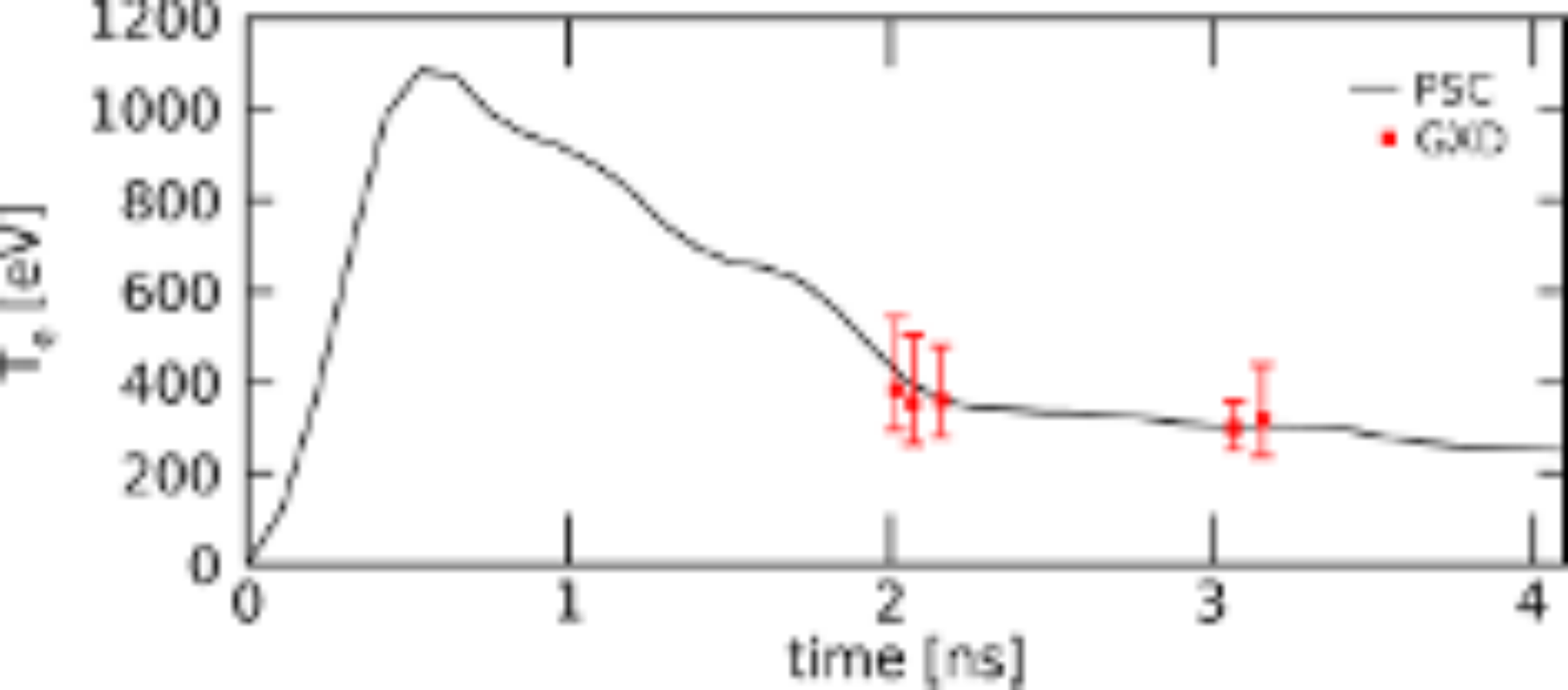
1200
1000
800
600
400
200
0
T_e [eV]
0
1
2
3
4
time [ns]
PSC
GXD

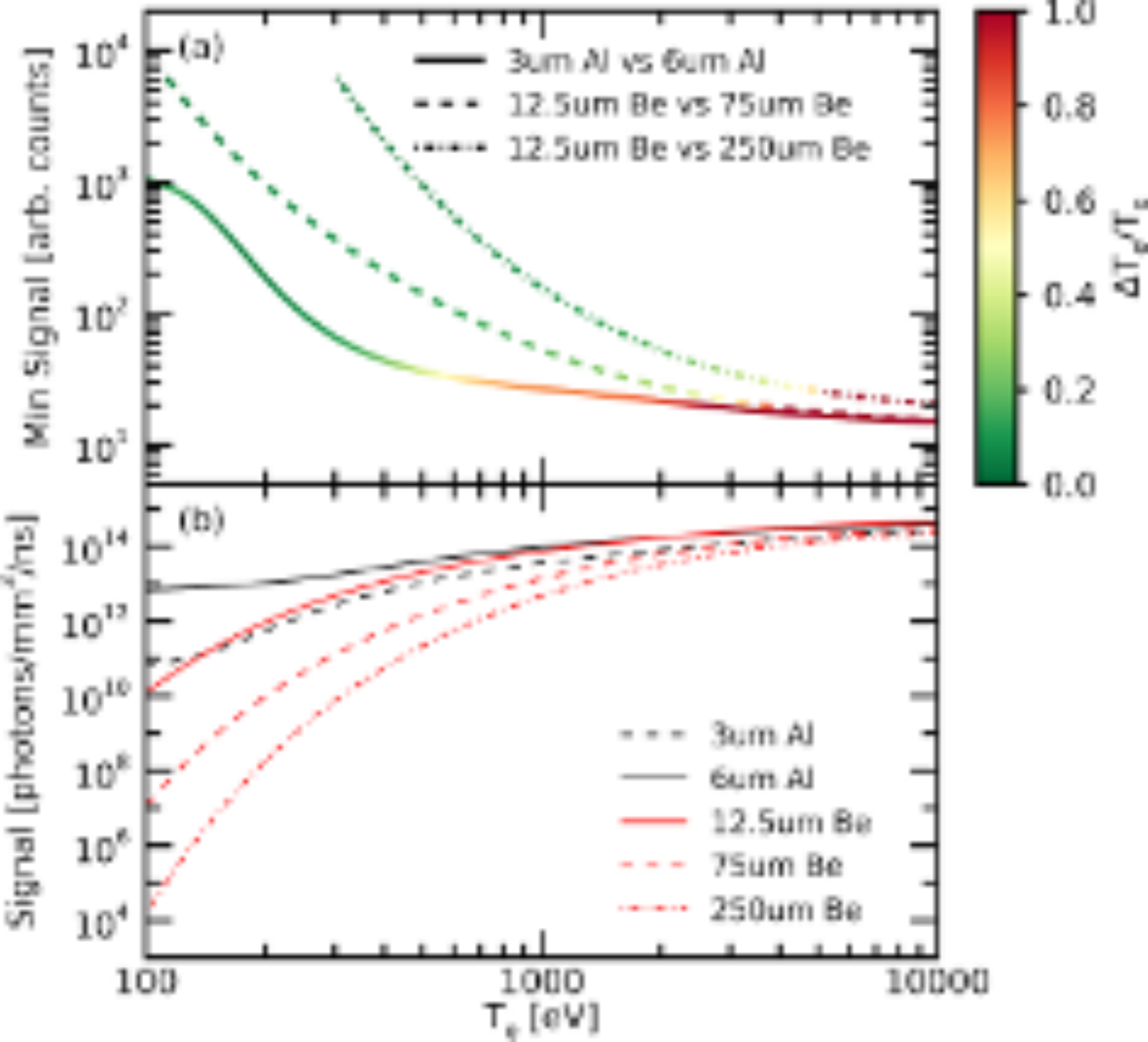
(a)
3um Al vs 6um Al
12.5um Be vs 75um Be
12.5um Be vs 250um Be
Min Signal [arb. counts]
10^4
10^3
10^2
10^1
1.0
0.8
0.6
0.4
0.2
0.0
$\Delta T_e/T_e$
(b)
Signal [photons/mm^2/ns]
10^{14}
10^{12}
10^{10}
10^8
10^6
10^4
3um Al
6um Al
12.5um Be
75um Be
250um Be
100
1000
10000
T_e [eV]